Chemical-genetic interaction mapping links carbon metabolism and cell wall structure to tuberculosis drug efficacy

Eun-Ik Koh[1], Peter O. Oluoch[1], Nadine Ruecker[2], Megan K. Proulx[1], Vijay Soni[2], Kenan C. Murphy[1], Kadamba G. Papavinasasundaram[1], Charlotte J. Reames[1], Carolina Trujillo[2], Anisha Zaveri[2], Matthew D. Zimmerman[3], Roshanak Aslebagh[4,5], Richard E. Baker[1], Scott A. Shaffer[4,5], Kristine M. Guinn[6], Michael Fitzgerald[7], Véronique A. Dartois[3,8], Sabine Ehrt[2], Deborah T. Hung[7,9,10], Thomas R. Ioerger[11], Eric Rubin[6], Kyu Y. Rhee[2], Dirk Schnappinger[2] and Christopher M. Sassetti[1]

[1] Department of Microbiology and Physiological Systems, University of Massachusetts Medical School, Worcester, Massachusetts, 01655 USA

[2] Department of Microbiology and Immunology, Weill Cornell Medical College, New York, New York, 10065 USA

[3] Center for Discovery and Innovation, Hackensack Meridian Health, Nutley, New Jersey, 07110 USA

[4] Department of Biochemistry and Molecular Pharmacology, University of Massachusetts Medical School, Worcester, Massachusetts, 01655 USA

[5] Mass Spectrometry Facility, University of Massachusetts Medical School, Shrewsbury, Massachusetts, 01545 USA

[6] Department of Immunology and Infectious Diseases, Harvard T.H. Chan School of Public Health, Boston, Massachusetts, 02115 USA

[7] Broad Institute of MIT and Harvard, Cambridge, Massachusetts, 02142 USA

[8] Department of Medical Sciences, Hackensack School of Medicine, Nutley, New Jersey, 07110 USA

[9] Department of Molecular Biology and Center for Computation and Integrative Biology, Massachusetts General Hospital, Boston, Massachusetts, 02114 USA

[10] Department of Genetics, Harvard Medical School, Boston, Massachusetts, 02114 USA

[11] Department of Computer Science and Engineering, Texas A&M University, College Station, Texas, 77840 USA

Corresponding author

Christopher M. Sassetti

368 Plantation Street, AS8-2051, Worcester, MA 01605

508-856-3678

Christopher.sassetti@umassmed.edu

Author contributions

Conceptualization, EK, CMS; Methodology, EK, NR, KCM, KGP, CJR, CT, AZ, REB, KMG, MF, SE, DTH, TRI, ER, DS, CMS; Investigation, EK, POO, MKP, VS, MDZ, RA, SAS, VAD, KYR; Analysis, EK, VS, MDZ, RA, SAS, VAD, KYR; Writing original draft, EK, CMS; Review and editing, all authors; Supervision, C.M.S

Competing interest statements

The authors declare no competing interests.

Classifications

Biological Sciences

Microbiology

Keywords

Mycobacterium tuberculosis, chemical-genetic interactions, carbon metabolism, antibiotics

Abstract

Current chemotherapy against *Mycobacterium tuberculosis (Mtb)*, an important human pathogen, requires a multidrug regimen lasting several months. While efforts have been made to optimize therapy by exploiting drug-drug synergies, testing new drug combinations in relevant host environments remains arduous. In particular, host environments profoundly affect the bacterial metabolic state and drug efficacy, limiting the accuracy of predictions based on *in vitro* assays alone. In this study, we utilize conditional *Mtb* knockdown mutants of essential genes as an experimentally-tractable surrogate for drug treatment, and probe the relationship between *Mtb* carbon metabolism and chemical-genetic interactions (CGI). We examined the anti-tubercular drugs isoniazid, rifampicin and moxifloxacin, and found that CGI are differentially responsive to the metabolic state, defining both environment-independent and –dependent interactions. Specifically, growth on the *in vivo*-relevant carbon source, cholesterol, reduced rifampicin efficacy by altering mycobacterial cell surface lipid composition. We report that a variety of perturbations in cell wall synthesis pathways restore rifampicin efficacy during growth on cholesterol, and that both environment-independent and cholesterol-dependent *in vitro* CGI could be leveraged to enhance bacterial clearance in the mouse infection model. Our findings present an atlas of novel chemical-genetic-environmental interactions that can be used to optimize drug-drug interactions as well as provide a framework for understanding *in vitro* correlates of *in vivo* efficacy.

78 **Significance**

79 Efforts to improve tuberculosis therapy include optimizing multi-drug regimens to take
80 advantage of drug-drug synergies. However, the complex host environment has a
81 profound effect on bacterial metabolic state and drug activity, making predictions of
82 optimal drug combinations difficult. In this study, we leverage a newly developed library
83 of conditional knockdown *Mycobacterium tuberculosis* mutants in which genetic
84 depletion of essential genes mimics the effect of drug therapy. This tractable system
85 allowed us to assess the effect of growth condition on predicted drug-drug interactions.
86 We found that these interactions can be differentially sensitive to the metabolic state
87 and select *in vitro*-defined interactions can be leveraged to accelerate bacterial killing
88 during infection. These findings suggest new strategies for optimizing tuberculosis
89 therapy.

90

91

92 **Introduction**

93 The current chemotherapeutic regimen for tuberculosis (TB) is the product of many
94 decades of basic and clinical research. Since the first trials of streptomycin
95 monotherapy in 1948 were rapidly followed by the emergence of antibiotic resistant
96 clones (1), multidrug regimens to both suppress resistance and accelerate bacterial
97 killing have become standard. The current regimen used against drug-sensitive strains
98 of *Mycobacterium tuberculosis* (*Mtb*) consists of four antibiotics, isoniazid (INH),
99 rifampicin (RIF), pyrazinamide (PZA), and ethambutol (EMB), and was optimized in a
100 series of clinical trials in the 1970s (2, 3). While this "short-course regimen" has been
101 credited with curing over 50 million patients, its delivery is complicated by the need for
102 6-9 months of drug administration (4). Furthermore, even in clinical trial settings where
103 the delivery of this extended regimen is assured, 5-10% of patients fail therapy (5). The
104 frequent transmission of antibiotic resistant *Mtb* strains has further complicated TB
105 treatment options, requiring the use of less optimized drug combinations that are
106 administered for even longer periods (6).

107

108 The factors that necessitate prolonged therapy are complex and specific to the infection
109 environment. While antibiotics such as INH and RIF cause rapid cell death *in vitro*, their
110 antimicrobial activities are much slower during infection (7). Limited drug penetration
111 into *Mtb*-containing tissue lesions may reduce the efficacy of some drugs. For example,
112 the intralesional RIF concentrations are significantly lower than what is achieved in the
113 plasma (8, 9), and clinical studies suggest that increased RIF dosing improves bacterial
114 clearance (10, 11). However, drug penetration is unlikely to fully account for the reduced

115 antibiotic efficacy in host tissue, as this complex and stressful environment has also
116 been shown to alter the physiology of the pathogen to induce a drug-tolerant state (12–
117 14). While a number of host immune-related stresses may be involved in this process,
118 simple changes in macronutrient availability can have important consequences. *Mtb* has
119 access to a mixture of glycolytic carbon sources, fatty acids and cholesterol in host
120 tissue (15–17), and altering the availability of these carbon sources *in vitro* can change
121 the efficacy of anti-tubercular compounds (18–23). A role for differential carbon
122 catabolism in determining drug efficacy is also supported by the identification of natural
123 genetic variants in clinical *Mtb* isolates that enhance drug tolerance by altering either
124 glycerol, lipid, or sterol catabolism (24, 25). The profound effect of the host environment
125 on bacterial metabolic state and drug activity makes it difficult to predict the ultimate
126 efficacy of an antibiotic regimen based on *in vitro* assays alone.
127
128 The most advanced efforts to accelerate TB therapy involve optimizing multi-drug
129 regimens to take advantage of drug-drug synergies. These pharmacological
130 interactions can improve therapy by increasing drug exposure, decreasing MIC, or
131 enhancing the maximal effect of the treatment (26). However, despite the demonstrated
132 benefits of synergistic regimens in many therapeutic realms, the combinatorial burden of
133 testing all potential multi-drug combinations remains cumbersome. While recent
134 advances to more efficiently predict synergies *in vitro* have proven valuable (27, 28), it
135 remains unclear whether the environmental influences that alter the efficacy of
136 individual drugs will also influence drug-drug interactions (29, 30).
137

138 In this study, we leveraged a newly developed genetic resource to understand the effect
139 of growth conditions on potential drug-drug interactions. This “hypomorph library”
140 consists of individually DNA barcoded strains in which individual essential genes are
141 tagged with the DAS+4 sequence that targets proteins for degradation upon inducible
142 induction of the SspB adapter (31). Graded *sspB* expression produces different degrees
143 of depletion to model the effect of partial chemical inhibition (32). This approach allowed
144 for highly parallel assessment of changes in TB drug sensitivity of individual
145 hypomorphic mutants under different growth conditions; creating a drug-specific
146 chemical-genetic interaction (CGI) profile (33). We report that drugs of distinct classes
147 produce interactions that are differentially sensitive to the environment, and that both
148 condition-independent and –dependent CGIs can be identified for all drugs tested. In
149 particular, RIF efficacy was impaired as a result of cell surface lipid alterations that
150 occur during growth in cholesterol, and the cell could be resensitized through a
151 condition-specific interaction with the cell wall synthetic machinery both *in vitro* and in
152 the mouse lung. These observations provide a compendium of chemical-genetic
153 interactions that can be exploited to enhance therapy and begin to define *in vitro*
154 correlates of *in vivo* efficacy.
155

156 **Results**

157 **Genetic strategy to define essential bacterial functions that alter drug efficacy *in***
158 ***vitro.***

159 Host environmental factors alter antibiotic efficacy against TB (12, 24, 34, 35). To
160 determine if carbon source availability specifically affects antibiotic efficacy, we used the

161 *Mtb* strain H37Rv in minimal medium with glycerol, acetate or cholesterol as sole
162 carbon sources in a growth inhibition assay with the TB drugs isoniazid (INH), rifampicin
163 (RIF) and moxifloxacin (MOX). As these carbon sources support different growth rates,
164 endpoint-based antibiotic activity measurements such as MIC assays can be difficult to
165 interpret. Therefore we quantified growth rates in each carbon source over multiple
166 concentrations of antibiotics to determine the concentration that decreased the growth
167 rate by 50% (GR_{50}) (24, 36). Growth of individual strains was monitored during
168 exponential phase (OD_{600} 0.20-0.25) and the growth rate was determined by fitting an
169 exponential curve **(Fig1A)**. We found different carbon sources to alter the GR_{50} of these
170 drugs in distinct ways. For INH, glycerol-dependent growth increased efficacy, relative
171 to the non-glycolytic carbon sources. In contrast, growth in cholesterol was found to
172 decrease RIF efficacy, relative to the other conditions. Media composition had a more
173 modest effect on MOX, altering GR_{50} by only approximately 2-fold **(Fig1B)**. These
174 findings show that carbon metabolism plays an important role in antibiotic efficacy and
175 has distinct effects on different drugs.
176
177 To understand the mechanisms linking drug efficacy and metabolism, we utilized a
178 barcoded-hypomorph library consisting of 465 essential genes to identify CGI with these
179 drugs (32). The library was grown in minimal media with glycerol, acetate or cholesterol,
180 and antibiotics were added at concentrations ranging from 0.05X to 1X GR_{50} for each.
181 Bacteria were subjected to these conditions in 96-well plates for 14 days, at which point
182 the relative abundance of individual mutants was assessed through multiplex PCR and
183 Next-Generation Sequencing **(Fig1C, S.Table 1)**. Relative abundances of individual

184 mutants were calculated by normalizing the mutant's barcode count to the total barcode
185 count and comparing the relative abundance of each mutant in different drug
186 concentrations with the untreated control samples.
187
188 We initially investigated the validity of this dataset by determining if genetic inhibition of
189 each drug's target produced the expected CGI with that compound in standard glycerol-
190 dependent growth conditions. RIF and MOX inhibit the RNA polymerase subunit, RpoB
191 or the DNA gyrase subunit, GyrA, respectively. As expected, *rpoB* and *gyrA*
192 hypomorphic mutants were hypersensitive to RIF or MOX, and the CGI increased with
193 drug concentration **(Fig1D)**. The major target of INH, InhA, was not present in our
194 mutant pool. However, the library did contain a *ndh* mutant. Deficiency in this NADH-
195 dehydrogenase is known to decrease INH efficacy, likely due to the inefficient formation
196 of the active INH-NAD adduct (37). Consistent with these observations, we found that
197 the *ndh* hypomorphic mutant showed an INH dose-dependent increase in abundance in
198 our dataset **(Fig1D)**.
199
200 The hypomorph library was constructed to contain up to five different versions of each
201 DAS+4 tagged mutant, which express different levels of *sspB* and therefore produce
202 graded levels of protein depletion (31, 38). To investigate the relationship between
203 target protein abundance and phenotype, we correlated the strength of *sspB* expression
204 with drug sensitivity for a number of genes that were expected to alter antibiotic efficacy
205 **(Fig1E)**. For RIF, we concentrated on *rpoB*. For INH, we examined *ndh* as well as
206 genes associated with mycolate biosynthesis, and found *kasA* and *hadB* mutants to be

207 significantly hypersensitive to increasing INH concentrations. For MOX, in addition to
208 *gyrA*, depletion of proteins associated with DNA integrity or deoxynucleotide production,
209 *dnaN*, *lexA* and *ndrF2,* showed significantly decreased fitness over increasing MOX
210 concentrations. For some mutants, particularly those involved in DNA metabolism, we
211 noted a dose-dependent effect of *sspB* expression, with larger phenotypes
212 corresponding to greater degrees of depletion. However, this was not a universal
213 phenomenon, and we often found that independent mutants expressing different *sspB*
214 levels produced consistent phenotypic effects. The observed differences in sensitivity to
215 protein depletion likely reflect the unique biochemistry of each pathway (39). As a result,
216 we considered each mutant corresponding to a target protein independently in the
217 following analyses.
218
219 **CGI profiles are determined by the combination of carbon source and drug**
220 To understand the relative importance of carbon metabolism and drug on bacterial
221 physiology, we compared the "fitness profiles" of each condition, which represented the
222 relative fitness of each mutant strain. We first selected the fold change in abundance
223 (log2FC) values of every mutant at 0.65X GR_{50} drug concentration that showed a
224 statistically significant fitness difference when at least one treated sample was
225 compared to the untreated control (918 mutants, Q <0.05). 0.65X GR_{50} drug
226 concentration displayed the largest number of mutants with a statistically significant
227 fitness difference across most conditions. Upon hierarchical clustering of both genes
228 and conditions, we found three major condition clusters that corresponded to each
229 antibiotic **(Fig2A)**. These condition clusters were differentiated by two distinct clusters of

230 mutants; one large gene set differentiated MOX from the other drugs (Fig 2A bottom
231 cluster), and differential fitness effects on a second smaller gene set differentiated INH
232 and RIF (Fig2A top cluster). Within each condition cluster, fitness effects due to carbon
233 source were apparent.
234
235 To catalog the genes that differentiate these conditions, we compared each drug-
236 treated sample (0.65X GR_{50}) with the corresponding untreated control and chose genes
237 with log2FC < -1 and $p < 0.05$ for each carbon source. For all antibiotics tested, there
238 were mutants that showed decreased fitness across all carbon sources as well as those
239 associated with a single carbon source **(Fig2B)**. Notably, MOX produced the largest
240 number of mutants with decreased fitness in a condition-independent manner, while
241 INH and RIF produced the largest number of mutants with decreased fitness during
242 acetate and cholesterol-dependent growth respectively. To more quantitatively assess
243 the relative contribution of carbon source and drug, we used Principal Component
244 Analysis (PCA) to examine the amount of variance contributed by each, concentrating
245 only on the INH and RIF conditions, which produced the most condition-specific effects.
246 PC1 aligned to distinguish the carbon sources, while PC2 differentiated among drug
247 treatments **(Fig2C)**. The first and second principal components accounted for 37.6%
248 and 23.7% respectively, of the overall variance across the 9 data sets, indicating that
249 drug and carbon source played a relatively equal role in shaping bacterial physiology.
250
251 **Condition-independent CGI can be reproduced with individual mutants.**

252 Genes found to alter antibiotic efficacy from the high-throughput hypomorph analysis
253 were validated using individual mutant strains. For initial validation studies, we
254 concentrated on mutants predicted to show drug-hypersensitivity under all media
255 conditions. We also replaced acetate with butyrate, as butyrate provided relatively
256 enhanced growth that allowed for robust validation. As these hypomorph mutants target
257 essential genes that may alter growth, we compared the relative growth rates of
258 individual mutants to WT in different carbon sources **(SFig1)**. Variability in growth rates
259 of mutants in different growth conditions led to the utilization of the growth rate inhibition
260 method described above to determine the RIF MIC. The repression of a drug's target is
261 thought to increase sensitivity to inhibition by reducing the fraction of the target that
262 needs to be inhibited to reduce growth (40). As such, we anticipated that drug target
263 inhibition would result in condition-independent effects. This prediction was verified
264 using a *rpoB* hypomorphic mutant, which our screening data predicted to increase RIF
265 efficacy in all carbon sources **(Fig3A)**. As such, we verified that this degree of RpoB
266 depletion decreased the RIF MIC by 4 to 16-fold in each of the three media conditions
267 **(Fig3A)**. In addition to known drug targets, a number of additional genes were predicted
268 to enhance RIF efficacy in a carbon source-independent manner, including the
269 transcriptional regulator, Rv0472c. This gene has been named, mycolic acid desaturase
270 regulator (*madR*), based on its specific effect on the mycolate-modifying *desA1* and
271 *desA2* genes (41). As we found for RpoB, MadR depletion sensitized the bacterium to
272 RIF in all tested carbon sources in the single strain assay **(Fig3B)**. Finally, to ensure the
273 specificity of these CGI, we investigated whether they could be reversed by specific
274 metabolite complementation. As predicted by the screen, depletion of the lysine

275 biosynthetic enzyme, LysA, produced RIF hypersensitivity in both glycerol and
276 cholesterol media, and we found this phenotype was largely reversed by
277 supplementation with 3mM lysine **(Fig3C)**. These data support the predictions of the
278 primary screen, and demonstrate that certain CGI are relatively unaffected by carbon
279 source.
280
281 **Depletion of cell-wall biosynthetic genes produces condition-specific RIF**
282 **interactions**
283 As cholesterol represents a primary carbon source for *Mtb* during infection (16, 42), and
284 RIF efficacy is thought to be limited by drug exposure (43–45), we probed the
285 hypomorph fitness profiles for clues to the mechanism underlying the cholesterol-
286 dependent increase in RIF MIC. We found that inhibition of genes associated with
287 different components of the mycobacterial cell wall, including arabinogalactan (*embC*
288 and *aftB*), and mycolic acid (*kasA*) (46, 47) preferentially sensitized the bacterium to RIF
289 during cholesterol growth **(Fig4A)**. These mutants were significantly underrepresented
290 by up to 8-fold upon RIF treatment predominantly in cholesterol growth conditions
291 across multiple *sspB* doses and drug concentrations. To further explore the effect of cell
292 wall inhibition, we tested individual mutants with defects in peptidoglycan (*dapE*),
293 arabinogalactan (*aftB*), and mycolic acid (*hadB*) synthesis (46, 48–50). We first
294 compared the relative growth rates of individual mutants to WT in different carbon
295 sources and found no significant differences for *dapE* and *hadB* hypomorph mutants
296 across all conditions, while *aftB* hypomorph mutant showed modest growth rate
297 increase in glycerol **(SFig2)**. We then found that perturbation in each of these cell wall

298 layers produced only relatively modest effects in glycerol or butyrate media, but all
299 consistently sensitized the bacterium to RIF in cholesterol growth conditions **(Fig4BCD)**.
300 These observations suggest that alterations in cell wall structure might underlie the
301 relationship between cholesterol catabolism and reduced RIF efficacy.
302
303 **RIF efficacy correlates with propionate catabolism and branched chain lipid**
304 **abundance.**
305 *Mtb* catabolizes cholesterol to pyruvate, propionyl-CoA and acetyl-CoA (17, 51).
306 Propionyl-CoA is a precursor of branched-chain lipid synthesis, and catabolism of either
307 cholesterol or propionate increases cellular propionyl-CoA levels causing an increase in
308 both the abundance and chain-length of cell wall lipids, such as diacyltrehalose (DAT),
309 polyacyltrehalose (PAT), and sulfolipid-1 (SL-1) (51–54). To understand whether these
310 alterations in cell wall lipids could be responsible for altering RIF efficacy, we compared
311 RIF GR_{50} values in cells grown in cholesterol to those grown in butyrate media
312 supplemented with increasing concentrations of propionate. Growth rate in cholesterol
313 showed no significant difference compared to both butyrate and butyrate supplemented
314 with propionate **(SFig3)**. We observed that GR_{50} values increased up to 8-fold with
315 increasing propionate levels, and the addition of 0.1X propionate, reflecting a 1:10 ratio
316 of propionate to butyrate (weight:weight), mimicked the effect of cholesterol **(Fig5A)**. To
317 more quantitatively associate branched-chain lipid abundance with drug efficacy, we
318 performed relative quantification of the abundance of SL-1 during growth in butyrate,
319 butyrate and propionate, and cholesterol using mass spectrometry. As expected, we
320 found that growth in either propionate or cholesterol increased both the *m/z* range of

321 SL-1 and its total abundance, and the effect of propionate was dose-dependent in the
322 tested range **(Fig5B)**. This dose-dependency allowed us to correlate changes in
323 sulfolipid abundance with changes in rifampicin efficacy. At multiple propionate
324 concentrations, we calculated the GR_{50} for RIF and the total abundance of SL-1. We
325 found a correlation between these values, as 0.003X propionate supplementation had
326 no effect on either SL-1 abundance or RIF GR_{50}, and 0.1X increased both values
327 **(Fig5C)**. These findings implied that the propionyl-CoA derived from cholesterol alters
328 rifampicin efficacy through modification of mycobacterial surface lipids.
329
330 The different branched chain lipid species of *Mtb* are produced by distinct biosynthetic
331 pathways, and inhibiting the synthesis of one lipid can produce a compensatory
332 increase in others (53). Therefore, to assess whether increased lipid abundance was
333 causally related to RIF efficacy, we employed an *Mtb* mutant lacking the PhoPR
334 regulatory system, which is required for the synthesis of multiple branched chain lipid
335 species (55–57). We first compared the relative growth rates of Δ*phoPR* deletion mutant
336 to WT in different carbon sources and found that while Δ*phoPR* deletion mutant showed
337 modest growth rate decrease in butyrate, no significant differences were seen in
338 butyrate with supplemented with propionate and cholesterol conditions **(SFig3)**. In
339 contrast to wild type *Mtb,* a Δ*phoPR* deletion mutant showed little change in rifampicin
340 efficacy with propionate supplementation or cholesterol compared to butyrate growth
341 conditions, and possessed significantly decreased SL-1 levels compared to WT
342 **(Fig6AB)**. Similar to the effects seen with the Δ*phoPR* mutant, cell wall defective
343 hypomorphs (*aftB, hadB, dapE*) also maintained a relatively consistent RIF GR50 in all

344 media conditions, compared to wild type **(Fig6CD)**. These findings suggest that
345 cholesterol catabolism reduces RIF efficacy via a propionyl-CoA driven increase in
346 synthesis of cell surface lipids, and that this effect can be reversed by perturbing the
347 structure of the cell envelope. We note that while depletion of AftB sensitized Mtb to RIF
348 and significantly decreased SL-1 abundance in both cholesterol- and propionate-
349 containing media, the correlation between these two effects was not absolute. AtfB
350 depletion decreased sulfolipid levels to differing degrees under these conditions
351 **(Fig6B)**. This implies that cell wall perturbation might be able to reverse the cholesterol-
352 and lipid-driven RIF resistance phenotype without directly altering lipid abundance.
353

354 ***In vitro* CGI predict drug efficacy *in vivo***

355 To determine whether CGI identified *in vitro* predict strategies to accelerate bacterial
356 killing in the lung, we infected C57BL/6J mice via the aerosol route with a pooled culture
357 consisting of 3 barcoded WT strains and a number of select hypomorph mutants. We
358 concentrated on genes that either displayed carbon source-independent increase in RIF
359 efficacy (*rpoB*, *madR*), or mutants that disrupt the peptidoglycan (*murA*) or
360 arabinogalactan (*aftB*) layer of the cells wall and would be expected to reverse the
361 effect of host-derived cholesterol catabolism **(Fig3AB, Fig4BC, S.Fig4)**. To ensure that
362 the animals were treated with a relevant dose of antibiotic, we measured the plasma
363 concentration of RIF in mice and adjusted the dosing to match the 24-hour exposure
364 observed during clinical TB therapy **(Fig7A)** (58). The mice were fed doxycycline chow
365 starting 3 days before infection to repress *sspB* expression in the mutants upon
366 infection, and allow them to grow normally. At 3 weeks post-infection, mice were split to

367 three groups. One group maintained doxycycline for the remainder of the infection
368 without RIF treatment (ND, non-depleted). A second group had doxycycline withdrawn
369 to initiate protein degradation for the remainder of the infection without RIF treatment
370 (D, depleted). The third group had doxycycline withdrawn and two weeks of RIF
371 treatment was administered (D+R, depleted and RIF treated) **(Fig7B)** (59). The
372 antibiotic regimen effectively decreased the total number of lung CFU **(Fig7C)**. Lung
373 homogenates were washed and plated on 7H10 plates with supplementation to recover
374 viable clones. The relative abundance of individual mutants was normalized to the
375 average abundance of three barcoded WT strains for each mouse and fitness changes
376 were calculated by comparing between conditions. Comparing groups D and ND show
377 the relative fitness effects of depletion alone on individual hypomorphs, while examining
378 groups D+R and D show the relative change in fitness due to RIF treatment across
379 depleted samples. Groups ND and D+R were compared to investigate the combined
380 impact of both depletion and RIF treatment.
381 RpoB, AftB and MurA depletion decreased fitness compared to non-depleted controls,
382 while MadR depletion increased relative fitness in the mouse model. Upon RIF
383 treatment, we found that AftB depletion increased bacterial clearance to the same
384 degree as RpoB depletion. Depleting MadR had an even greater effect, and the
385 abundance of this mutant was reduced below our limit of detection in eleven out of
386 twelve animals **(Fig7D)**. The effect of MurA depletion was more variable and its effect
387 on RIF efficacy was not statistically significant. In sum, the reproducible effects of RpoB,
388 AtfB, and MadR on RIF efficacy show that CGI identified *in vitro* can accelerate bacterial

389 clearance during infection, and highlight the importance of the environment for defining
390 relevant interactions.
391
392 **Discussion**
393 Optimizing combination therapy is critical to improving TB treatment. While efficient
394 strategies for predicting and quantifying drug-drug interactions under *in vitro* conditions
395 have been developed, the impact of bacterial environment on these interactions has not
396 been determined (27, 28). As a result, it remains unclear how well these *in vitro* data
397 predict the effects of combination therapy in the infection environment. In this study, we
398 modeled drug-drug interactions using a newly developed genetic hypomorph library to
399 assess the impact of bacterial carbon metabolism on CGI. This work revealed that CGI
400 with distinct drugs are differentially sensitive to the environment, suggesting tailored
401 approaches to optimization.
402
403 While global analysis of our chemical-genetic-environmental dataset suggested that
404 drug mechanism and environment both play critical roles in shaping chemical-genetic
405 interactions, all drugs were not equally affected by condition. In particular, the individual
406 effect of the fluoroquinolone, MOX, was unaffected by carbon source, and this relative
407 indifference to the environment was also observed for CGI with MOX. These
408 observations contrast with RIF and INH, where carbon source plays an important role in
409 determining the MIC of the drug alone, as well as shaping chemical-genetic interaction
410 profiles. While we can only speculate on the mechanistic basis for these differences
411 between drugs, we found that the cholesterol-dependent decrease in RIF sensitivity is

412 due to the effect of carbon source on cell envelope structure that is likely to alter RIF
413 penetration. Similarly, the activation of the prodrug, INH, is affected by the redox state
414 of the cell (60), another process that is impacted by carbon catabolism. In contrast,
415 MOX is not a prodrug and we speculate that it may not be limited by cellular penetration
416 as strongly as RIF. More practically, these observations suggest that drug-drug
417 interactions with MOX may be particularly robust to changes in condition, and therefore
418 may translate well between *in vitro* and *in vivo* conditions.
419
420 Complex drug-drug interactions may both increase or decrease sensitivity. Our dataset
421 found potential antagonistic interactions that may arise with different TB antibiotics. For
422 example, the inhibition of Ndh, a NADH-dehydrogenase, has previously been shown to
423 decrease INH efficacy and was also identified in our dataset (37). Antagonistic
424 interactions have important implications for TB therapeutics due to the reliance on multi-
425 drug regimens, and our study provides a global assessment of these effects.
426
427 While RIF interactions were complex and condition-dependent compared to MOX, we
428 found that the cholesterol-specific effects translate well to the infection environment and
429 may be particularly relevant to treatment. As reduced RIF exposure limits the efficacy of
430 this critical component of our standard regimen, even small increases in MIC during
431 infection could have a significant effect on bacterial killing. A number of observations
432 indicate that RIF efficacy is limited by similar mechanisms *in vivo* and in cholesterol-
433 containing media. Firstly, the increase in branched-chain lipid abundance that is
434 associated with reducing RIF efficacy in cholesterol- or propionate-containing media has

435 also been observed during infection, where similar carbon sources are utilized (16, 53).
436 Furthermore, genetic perturbation of the same cell wall synthetic enzymes sensitized
437 Mtb to RIF in both conditions. This effect may underlie the increased cell-associated RIF
438 upon simultaneous INH and ethambutol treatment *in vitro* (61–63). While the importance
439 of cell wall architecture and cell envelope lipid production suggests that cellular
440 permeability to RIF may be altered during growth on cholesterol, we note that lipid
441 synthesis also has important effects on central carbon metabolic pathways that could
442 influence antibiotic susceptibility (15). Furthermore, the mixture of carbon sources
443 available in different host microenvironments remains ill-defined, and cholesterol may
444 not be the only macronutrient capable of limiting RIF efficacy. Additional enzymes
445 identified in this study may also be attractive targets for further drug development, such
446 as AftB, a arabinofuranosyltransferase distinct from EmbA and EmbB that are targets
447 of ethambutol (47). Similarly, enzymes in the DAP (diaminopimelic acid) biosynthesis
448 pathway produce precursors for the synthesis of peptidoglycan and lysine (64), and the
449 loss of either sensitizes the cell to RIF.
450
451 Using a chemical-genetic system, we determined that cellular environment plays an
452 important role in shaping CGIs, and that even the use of relatively simple *in vitro* culture
453 conditions can identify interactions that are relevant during infection. These studies
454 provide a tractable system that can incorporate more complex culture systems, or even
455 cellular models, to identify additional *in vivo*-relevant interactions. Expanding this CGI
456 atlas promises to elucidate the processes limiting drug efficacy during infection and
457 guide drug development and regiment optimization efforts.

458

459 **Material and methods**

460 **Bacterial cultures**

461 *M. tuberculosis* (H37Rv) cells were cultured in Middlebrook 7H9 medium supplemented
462 with 10% oleic acid-albumin-dextrose-catalase (OADC), 0.5% glycerol, and 0.05%
463 Tween-80, or in minimal medium supplemented with 0.1% Tyloxapol and variable levels
464 of glycerol, acetate, butyrate, propionate, or cholesterol up to 0.1%. Minimal medium
465 was made as previously described but with ferric chloride (100uM) replacing ferric
466 ammonium citrate (51).
467 Cells were also cultured on 7H10 agar medium supplemented with 10% OADC and
468 0.5% glycerol. Streptomycin (20ug/mL) was supplemented when necessary.
469 Anhydrotetracycline (ATC, 500ng/mL) was supplemented periodically until cultures
470 reach exponential growth. ATC was removed from cultures prior to antibiotic growth
471 inhibition assays by washing in PBS supplemented with 0.1% Tyloxapol. *ΔphoPR*
472 mutant was generated as described previously (65).

473

474 **Multiplexed library screening**

475 Library pools of hypomorph mutants were prepared as described previously (32). Pools
476 were initially cultured in Middlebrook 7H9 medium supplemented with 10% oleic acid-
477 albumin-dextrose-catalase (OADC), 0.5% glycerol, and 0.05% Tween-80. Cultures were
478 supplemented with Anhydrotetracycline (ATC, 500ng/mL) periodically until cultures
479 reach exponential growth. ATC was removed from cultures by washing in PBS
480 supplemented with 0.1% Tyloxapol prior to inoculation in 96-well plates to allow

481 induction of SspB. Pools were grown in minimal medium with 0.1% glycerol, 0.1%
482 acetate, or 0.1% cholesterol on 96-well plates for 2 weeks. Isoniazid and moxifloxacin
483 were used at 1ug/mL and rifampicin was used at 0.062 ug/mL. Antibiotics were added
484 to select wells and serially diluted in a 2-fold manner prior to inoculation. An untreated
485 growth condition was included for each study. Samples were inoculated at OD600 0.01
486 and growth was monitored using OD600. Upon completion, 96-well plates were heat-
487 inactivated at 85 degrees for 2 hours. Barcodes were PCR amplified as described
488 previously (32). Individual libraries were mixed with 1:1 20% DMSO and heated for 10
489 minutes at 98 degrees prior to PCR reaction. Amplified barcodes were purified using
490 SPRI-based purification methods and sequenced using Next-generation sequencing
491 methods. Sequence alignment and analysis were conducted using Bowtie software
492 package with index mismatch set to 2 bases and barcode mismatch set to 1 base.
493 Relative abundance of every mutant was calculated as mean ratio of barcode
494 abundance of mutant relative to total barcode abundance of library. Log2FC of a mutant
495 was calculated as the log2 of the ratio of the mean relative abundances in a given
496 antibiotic condition relative to its untreated control. Hierarchical clustering and principal
497 component analysis were conducted using ClustVis (66). Hierarchical clustering was
498 applied to vectors of Log2FC of each gene across all conditions. PCA was performed
499 on relative abundances across all conditions. Statistical significance was determined by
500 unpaired *t*-test with Benjamini-Hochberg multiple testing correction.
501
502 **Antibiotic growth inhibition assay**

503 *Mtb* cells were grown in minimal medium with 0.1% glycerol, 0.01% acetate, 0.01%
504 butyrate, 0.01% propionate, or 0.01% cholesterol on 96-well plates. Isoniazid and
505 moxifloxacin were used at 1ug/ml and rifampicin was used at 0.062 ug/mL. Antibiotics
506 were added to select wells and serially diluted in a 2-fold manner prior to inoculation.
507 Untreated condition was included for each study. Cells were inoculated at OD600 0.01
508 and growth was monitored using OD600 until exponential phase (OD600 0.20-0.25).
509 Antibiotic efficacy was determined using growth rate inhibition as done previously (24).
510 The exponential growth constant (*k*) value was calculated by plotting an exponential
511 curve over all growth points. The *k*-value of each antibiotic concentration was
512 normalized to the *k*-value of the no-drug control. The GR_{50} value was defined as the
513 concentration of antibiotic that resulted in 50% decrease in growth rate. L-lysine (Sigma)
514 was added to growth conditions to final concentration of 3mM.
515
516 **Lipid extraction and mass spectrometry**
517 *Mtb* cells were grown in minimal medium with 0.01% butyrate, propionate or cholesterol.
518 Cells were inoculated at OD600 0.1 and grown to final OD600 of 0.7. Cells were
519 pelleted and heat-inactivated at 85 degrees for 45 minutes. Cells were washed in 10%
520 glycerol to remove residual detergents from growth media. Lipid extraction was
521 conducted with methyl tert-butyl ether (MTBE) as described previously (67). 1.5mL
522 methanol and 5mL MTBE were mixed with the cell pellet and placed into a glass tube
523 with a Teflon-lined cap. The mixture was incubated at room temperature for 5 hours
524 while shaking. Phase-separation was achieved by adding 0.75mL water to the tubes,
525 incubating for 10 minutes at room temperature, then centrifuging at 1000g for 10

526 minutes. The 2.5mL of the top phase was collected and transferred to a fresh glass tube
527 with Teflon-lined cap. Samples were dried using a nitrogen evaporator and stored in -20
528 degrees prior to injection to mass spectrometer. After evaporation of MTBE, 300 µL of
529 2:1 methanol:chloroform was added to each tube followed by vigorous vortex.
530 Solubilized lipids were then transferred to a new, pre-weighed tube, dried using a
531 nitrogen evaporator, and then tubes were re-weighed to determine the lipid mass in
532 each sample. Then 1.5 µL of 100 ng/µL N-omega-CD_3-octadecanoyl
533 monosialoganglioside GM_2 (Matreya, State College, PA) was added to each sample for
534 normalization and samples were reconstituted in 300 µL of 2:1 methanol: chloroform for
535 mass spectrometry analysis.
536 Samples were analyzed by direct infusion on a syringe pump to an Orbitrap Velos Pro
537 (Thermo Fisher Scientific, Waltham, MA) mass spectrometer operating in the negative
538 electrospray ionization mode. Mass spectra were acquired at a flow rate of 10 µL/min for
539 2 minutes in two different mass ranges, *m/z* 200-2000 and *m/z* 300-3000, acquiring two
540 replicates for each range using a resolution of 30,000 (*m/z* 200), an AGC target population
541 of $5e^5$ and a maximum ion injection time of 100 ms. Data were analyzed in Xcalibur 2.2
542 (Thermo Scientific). Briefly, mass spectra were averaged over the entire acquisition range
543 (0-2 minutes), producing one averaged spectrum for each analysis. Peak lists were
544 exported in Excel and intensity data was normalized to the intensity of the GM2
545 ganglioside spike.
546
547 **Plasma pharmacokinetic analysis**

548 C57BL/6J mice were purchased from Jackson Laboratories. Housing and
549 experimentation were done in accordance with the guidelines set by the Department of
550 Animal Medicine of University of Massachusetts Medical School and Institutional Animal
551 Care and Use Committee and adhered to the laws of the United States and regulations
552 of the Department of Agriculture. Eight- to 12-week mice were administered 0.1g/L RIF
553 through drinking water for three days. Blood was collected during a 12-hour period 24
554 hours post RIF administration, kept on ice, centrifuged at approximately 2500 x g for 5
555 minutes. After centrifugation, plasma was collected and stored at -80°C until analysis.
556 Neat 1 mg/mL DMSO stocks for RIF were serial diluted in 50/50 acetonitrile/water to
557 create neat spiking stocks. Standards and quality control (QC) samples were created by
558 adding 10 µL of spiking stock to 90 µL of drug free plasma. Ten microliters of control,
559 standard, QC, or study sample were added to 100 µL of acetonitrile/methanol 50/50
560 protein precipitation solvent containing 20 ng/mL RIF-d8. Extracts were vortexed for 5
561 minutes and centrifuged at 4000 RPM for 5 minutes. 100 µL of supernatant was combined
562 with 5 µL of 75 mg/mL ascorbic acid to stabilize RIF. 100 µL of mixture was combined
563 with 100 µL of Milli-Q water prior to HPLC-MS/MS analysis. Mouse control plasma
564 (K2EDTA) was sourced from Bioreclamation. Mouse control lungs were collected in
565 house. RIF was sourced from Sigma Aldrich and RIF-d8 was purchased from Toronto
566 Research Chemicals.
567 LC-MS/MS analysis was performed on a Sciex Applied Biosystems Qtrap 6500+ triple-
568 quadrupole mass spectrometer coupled to a Shimadzu Nexera X2 UHPLC system to
569 quantify each drug in plasma. Chromatography was performed on a Agilent SB-C8
570 (2.1x30 mm; particle size, 3.5 µm) using a reverse phase gradient. Milli-Q deionized water

571 with 0.1% formic acid was used for the aqueous mobile phase and 0.1% formic acid in
572 acetonitrile for the organic mobile phase. Multiple-reaction monitoring of
573 precursor/product transitions in electrospray positive-ionization mode was used to
574 quantify the analytes. Sample analysis was accepted if the concentrations of the quality
575 control samples were within 20% of the nominal concentration. The compounds were
576 ionized using ESI positive mode ionization and monitored using masses RIF
577 (823.50/791.60) and RIF-d8 (831.50/799.60). Data processing was performed using
578 Analyst software (version 1.6.2; Applied Biosystems Sciex).
579
580 ***In vivo* antibiotic susceptibility**
581 C57BL/6J mice were purchased from Jackson Laboratories. Housing and
582 experimentation were done in accordance with the guidelines set by the Department of
583 Animal Medicine of University of Massachusetts Medical School and Institutional Animal
584 Care and Use Committee and adhered to the laws of the United States and regulations
585 of the Department of Agriculture. Eight- to 12-week mice were infected with pools of
586 strains at equal ratios through the aerosol route (500 to 1000 CFU/mouse). Mice were
587 fed doxycycline-containing chow (Purina 5001 with 2000 ppm doxycycline, Research
588 Diets C11300-2000i) starting 3 days pre-infection to 21 days post-infection. At 21 days
589 post-infection, 0.1g/L rifampicin was administered through drinking water for 14 days. At
590 35 days post-infection, mice were sacrificed, spleen and lungs were isolated and
591 homogenized, and CFU was determined by plating dilutions on 7H10 agar with 50ug/mL
592 streptomycin and 500ng/mL ATC. For library recovery, approximately 1 million CFU per
593 mouse were plated on 7H10 agar with 50ug/mL streptomycin and 500ng/ml ATC.

594 Genomic DNA was extracted and normalized as done previously (35) and sequenced
595 using multiplex PCR methods. Sequence alignment and analysis were conducted using
596 Bowtie software package as described above. Relative abundance of every mutant was
597 calculated as mean ratio of barcode abundance of mutant relative to the average
598 barcode abundance of three barcoded H37Rv strains. Log2FC of a mutant was
599 calculated as the log2 of the ratio of the mean relative abundances of rifampicin treated
600 mice relative to the untreated mice. Statistical significance was determined by unpaired
601 *t*-test.
602
603

Acknowledgements

We are thankful to the members of the Sassetti lab for both technical assistance and helpful discussion. We thank Sovie Lavalette-Levy and Curtis Engelhart for technical help. This work was supported by the Office of the Assistant Secretary of Defense for Health Affairs through the Peer Reviewed Medical Research Program, Focused Program Award, under award no. W81XWH-17-1-0692. Opinions, interpretations, conclusions, and recommendations are those of the author and are not necessarily endorsed by the Department of Defense. The work was additionally supported by the NIH (AI095208). Model figures were created with BioRender.com

614 1. , Streptomycin Treatment of Pulmonary Tuberculosis. *Br. Med. J.* **2**, 769–782 (1948).

615 2. W. Fox, D. Mitchison, Short-course chemotherapy for pulmonarytuberculosis. *Am Rev*
616 *Respir Dis* **111**, 325–353 (1975).

617 3. World Health Organization, *Guidelines for treatment of tuberculosis, 4th edition* (World
618 Health Organization, 2010).

619 4. World Health Organization, *Global tuberculosis report 2020.* (World Health
620 Organization, 2020).

621 5. S. H. Gillespie, *et al.*, Four-Month Moxifloxacin-Based Regimens for Drug-Sensitive
622 Tuberculosis. *http://dx.doi.org/10.1056/NEJMoa1407426* (2014)
623 https:/doi.org/10.1056/NEJMoa1407426 (November 4, 2020).

624 6. P. Nahid, *et al.*, Treatment of Drug-Resistant Tuberculosis. An Official
625 ATS/CDC/ERS/IDSA Clinical Practice Guideline. *Am. J. Respir. Crit. Care Med.* **200**, e93–
626 e142 (2019).

627 7. J. E. Gomez, J. D. McKinney, M. tuberculosis persistence, latency, and drug tolerance.
628 *Tuberculosis* **84**, 29–44 (2004).

629 8. A. A. Ordonez, *et al.*, Dynamic imaging in patients with tuberculosis reveals
630 heterogeneous drug exposures in pulmonary lesions. *Nat. Med.* **26**, 529–534 (2020).

631 9. M. C. Kjellsson, *et al.*, Pharmacokinetic Evaluation of the Penetration of
632 Antituberculosis Agents in Rabbit Pulmonary Lesions. *Antimicrob. Agents Chemother.*
633 **56**, 446–457 (2012).

634 10. R. J. Svensson, *et al.*, Greater Early Bactericidal Activity at Higher Rifampicin Doses
635 Revealed by Modeling and Clinical Trial Simulations. *J. Infect. Dis.* **218**, 991–999
636 (2018).

637 11. M. J. Boeree, *et al.*, High-dose rifampicin, moxifloxacin, and SQ109 for treating
638 tuberculosis: a multi-arm, multi-stage randomised controlled trial. *Lancet Infect. Dis.*
639 **17**, 39–49 (2017).

640 12. S.-H. Baek, A. H. Li, C. M. Sassetti, Metabolic regulation of mycobacterial growth and
641 antibiotic sensitivity. *PLoS Biol.* **9**, e1001065 (2011).

642 13. K. N. Adams, *et al.*, Drug Tolerance in Replicating Mycobacteria Mediated by a
643 Macrophage-Induced Efflux Mechanism. *Cell* **145**, 39–53 (2011).

644 14. Y. Liu, *et al.*, Immune activation of the host cell induces drug tolerance in
645 Mycobacterium tuberculosis both in vitro and in vivo. *J. Exp. Med.* **213**, 809–825
646 (2016).

647 15. R. R. Lovewell, C. M. Sassetti, B. C. VanderVen, Chewing the fat: lipid metabolism and
648 homeostasis during M. tuberculosis infection. *Curr. Opin. Microbiol.* **29**, 30–36 (2016).

649 16. A. K. Pandey, C. M. Sassetti, Mycobacterial persistence requires the utilization of host
650 cholesterol. *Proc. Natl. Acad. Sci. U. S. A.* **105**, 4376–4380 (2008).

651 17. A. D. Baughn, K. Y. Rhee, Metabolomics of Central Carbon Metabolism in
652 Mycobacterium tuberculosis. *Microbiol. Spectr.* **2** (2014).

653 18. D. A. Aguilar-Ayala, *et al.*, Antimicrobial activity against Mycobacterium tuberculosis
654 under in vitro lipid-rich dormancy conditions. *J. Med. Microbiol.* **67**, 282–285 (2018).

655 19. J. J. Baker, R. B. Abramovitch, Genetic and metabolic regulation of Mycobacterium
656 tuberculosis acid growth arrest. *Sci. Rep.* **8**, 1–16 (2018).

657 20. S. G. Franzblau, *et al.*, Comprehensive analysis of methods used for the evaluation of
658 compounds against Mycobacterium tuberculosis. *Tuberculosis* **92**, 453–488 (2012).

659 21. K. Pethe, *et al.*, A chemical genetic screen in Mycobacterium tuberculosis identifies
660 carbon-source-dependent growth inhibitors devoid of in vivo efficacy. *Nat. Commun.* **1**,
661 1–8 (2010).

662 22. P. Gopal, *et al.*, Pyrazinamide Resistance Is Caused by Two Distinct Mechanisms:
663 Prevention of Coenzyme A Depletion and Loss of Virulence Factor Synthesis. *ACS*
664 *Infect. Dis.* **2**, 616–626 (2016).

665 23. N. P. Kalia, *et al.*, Carbon metabolism modulates the efficacy of drugs targeting the
666 cytochrome bc1:aa3 in Mycobacterium tuberculosis. *Sci. Rep.* **9** (2019).

667 24. M. M. Bellerose, *et al.*, Common Variants in the Glycerol Kinase Gene Reduce
668 Tuberculosis Drug Efficacy. *mBio* **10**, e00663-19 (2019).

669 25. N. D. Hicks, *et al.*, Clinically prevalent mutations in Mycobacterium tuberculosis alter
670 propionate metabolism and mediate multidrug tolerance. *Nat. Microbiol.* **3**, 1032–
671 1042 (2018).

672 26. G. R. Zimmermann, J. Lehár, C. T. Keith, Multi-target therapeutics: when the whole is
673 greater than the sum of the parts. *Drug Discov. Today* **12**, 34–42 (2007).

674 27. M. Cokol, N. Kuru, E. Bicak, J. Larkins-Ford, B. B. Aldridge, Efficient measurement and
675 factorization of high-order drug interactions in Mycobacterium tuberculosis. *Sci. Adv.*
676 **3**, e1701881 (2017).

677 28. S. Ma, *et al.*, Transcriptomic Signatures Predict Regulators of Drug Synergy and Clinical
678 Regimen Efficacy against Tuberculosis. *mBio* **10** (2019).

679 29. J. Pasipanodya, T. Gumbo, An Oracle: Antituberculosis Pharmacokinetics-
680 Pharmacodynamics, Clinical Correlation, and Clinical Trial Simulations To Predict the
681 Future. *Antimicrob. Agents Chemother.* **55**, 24–34 (2011).

682 30. E. Nuermberger, C. Sizemore, K. Romero, D. Hanna, Toward an Evidence-Based
683 Nonclinical Road Map for Evaluating the Efficacy of New Tuberculosis (TB) Drug
684 Regimens: Proceedings of a Critical Path to TB Drug Regimens-National Institute of
685 Allergy and Infectious Diseases In Vivo Pharmacology Workshop for TB Drug
686 Development. *Antimicrob. Agents Chemother.* **60**, 1177–1182 (2016).

687 31. J.-H. Kim, *et al.*, Protein inactivation in mycobacteria by controlled proteolysis and its
688 application to deplete the beta subunit of RNA polymerase. *Nucleic Acids Res.* **39**,
689 2210–2220 (2011).

690 32. E. O. Johnson, *et al.*, Large-scale chemical–genetics yields new M. tuberculosis inhibitor
691 classes. *Nature* **571**, 72–78 (2019).

692 33. A. B. Parsons, *et al.*, Exploring the Mode-of-Action of Bioactive Compounds by
693 Chemical-Genetic Profiling in Yeast. *Cell* **126**, 611–625 (2006).

694 34. J. M. Stokes, A. J. Lopatkin, M. A. Lobritz, J. J. Collins, Bacterial Metabolism and
695 Antibiotic Efficacy. *Cell Metab.* **30**, 251–259 (2019).

696 35. M. M. Bellerose, *et al.*, Distinct Bacterial Pathways Influence the Efficacy of Antibiotics
697 against Mycobacterium tuberculosis. *mSystems* **5** (2020).

698 36. M. Hafner, M. Niepel, M. Chung, P. K. Sorger, Growth rate inhibition metrics correct for
699 confounders in measuring sensitivity to cancer drugs. *Nat. Methods* **13**, 521–527
700 (2016).

701 37. A. S. G. Lee, A. S. M. Teo, S.-Y. Wong, Novel Mutations in ndh in Isoniazid-Resistant
702 Mycobacterium tuberculosis Isolates. *Antimicrob. Agents Chemother.* **45**, 2157–2159
703 (2001).

704 38. J.-H. Kim, *et al.*, A genetic strategy to identify targets for the development of drugs that
705 prevent bacterial persistence. *Proc. Natl. Acad. Sci.* **110**, 19095–19100 (2013).

706 39. J.-R. Wei, *et al.*, Depletion of antibiotic targets has widely varying effects on growth.
707 *Proc. Natl. Acad. Sci.* **108**, 4176–4181 (2011).

708 40. G. Giaever, *et al.*, Genomic profiling of drug sensitivities via induced haploinsufficiency.
709 *Nat. Genet.* **21**, 278–283 (1999).

710 41. E. J. Peterson, *et al.*, Path-seq identifies an essential mycolate remodeling program for
711 mycobacterial host adaptation. *Mol. Syst. Biol.* **15** (2019).

712 42. R. V. der Geize, *et al.*, A gene cluster encoding cholesterol catabolism in a soil
713 actinomycete provides insight into Mycobacterium tuberculosis survival in
714 macrophages. *Proc. Natl. Acad. Sci.* **104**, 1947–1952 (2007).

715 43. A. H. Diacon, *et al.*, Early Bactericidal Activity of High-Dose Rifampin in Patients with
716 Pulmonary Tuberculosis Evidenced by Positive Sputum Smears. *Antimicrob. Agents*
717 *Chemother.* **51**, 2994–2996 (2007).

718 44. E. Chigutsa, *et al.*, Impact of Nonlinear Interactions of Pharmacokinetics and MICs on
719 Sputum Bacillary Kill Rates as a Marker of Sterilizing Effect in Tuberculosis.
720 *Antimicrob. Agents Chemother.* **59**, 38–45 (2015).

721 45. J. G. Pasipanodya, *et al.*, Serum Drug Concentrations Predictive of Pulmonary
722 Tuberculosis Outcomes. *J. Infect. Dis.* **208**, 1464–1473 (2013).

723 46. M. Jankute, J. A. G. Cox, J. Harrison, G. S. Besra, Assembly of the Mycobacterial Cell Wall.
724 *Annu. Rev. Microbiol.* **69**, 405–423 (2015).

725 47. M. Seidel, *et al.*, Identification of a Novel Arabinofuranosyltransferase AftB Involved in
726 a Terminal Step of Cell Wall Arabinan Biosynthesis in Corynebacterianeae, such as
727 Corynebacterium glutamicum and Mycobacterium tuberculosis. *J. Biol. Chem.* **282**,
728 14729–14740 (2007).

729 48. V. Usha, *et al.*, Reconstruction of diaminopimelic acid biosynthesis allows
730 characterisation of Mycobacterium tuberculosis N -succinyl-L,L-diaminopimelic acid
731 desuccinylase. *Sci. Rep.* **6**, 1–10 (2016).

732 49. M. Jankute, *et al.*, Disruption of Mycobacterial AftB Results in Complete Loss of
733 Terminal β(1 → 2) Arabinofuranose Residues of Lipoarabinomannan. *ACS Chem. Biol.*
734 **12**, 183–190 (2017).

735 50. C. Lefebvre, *et al.*, HadD, a novel fatty acid synthase type II protein, is essential for
736 alpha- and epoxy-mycolic acid biosynthesis and mycobacterial fitness. *Sci. Rep.* **8**, 1–15
737 (2018).

738 51. J. E. Griffin, *et al.*, Cholesterol Catabolism by Mycobacterium tuberculosis Requires
739 Transcriptional and Metabolic Adaptations. *Chem. Biol.* **19**, 218–227 (2012).

740 52. M. Jackson, G. Stadthagen, B. Gicquel, Long-chain multiple methyl-branched fatty acid-
741 containing lipids of Mycobacterium tuberculosis: Biosynthesis, transport, regulation
742 and biological activities. *Tuberculosis* **87**, 78–86 (2007).

743 53. M. Jain, *et al.*, Lipidomics reveals control of Mycobacterium tuberculosis virulence
744 lipids via metabolic coupling. *Proc. Natl. Acad. Sci.* **104**, 5133–5138 (2007).

745 54. X. Yang, N. M. Nesbitt, E. Dubnau, I. Smith, N. S. Sampson, Cholesterol Metabolism
746 Increases the Metabolic Pool of Propionate in M. tuberculosis. *Biochemistry* **48**, 3819–
747 3821 (2009).

748 55. S. B. Walters, *et al.*, The Mycobacterium tuberculosis PhoPR two-component system
749 regulates genes essential for virulence and complex lipid biosynthesis. *Mol. Microbiol.*
750 **60**, 312–330 (2006).

751 56. J. G. Asensio, *et al.*, The Virulence-associated Two-component PhoP-PhoR System
752 Controls the Biosynthesis of Polyketide-derived Lipids in Mycobacterium tuberculosis.
753 *J. Biol. Chem.* **281**, 1313–1316 (2006).

754 57. J. J. Baker, B. K. Johnson, R. B. Abramovitch, Slow growth of Mycobacterium
755 tuberculosis at acidic pH is regulated by phoPR and host-associated carbon sources.
756 *Mol. Microbiol.* **94**, 56–69 (2014).

757 58. K. E. Stott, *et al.*, Pharmacokinetics of rifampicin in adult TB patients and healthy
758 volunteers: a systematic review and meta-analysis. *J. Antimicrob. Chemother.* **73**,
759 2305–2313 (2018).

760 59. M. Gengenbacher, *et al.*, Tissue Distribution of Doxycycline in Animal Models of
761 Tuberculosis. *Antimicrob. Agents Chemother.* **64** (2020).

762 60. N. L. Wengenack, H. M. Hoard, F. Rusnak, Isoniazid Oxidation by Mycobacterium
763 tuberculosis KatG: A Role for Superoxide Which Correlates with Isoniazid
764 Susceptibility. *J. Am. Chem. Soc.* **121**, 9748–9749 (1999).

765 61. M. B. McNeil, S. Chettiar, D. Awasthi, T. Parish, Cell wall inhibitors increase the
766 accumulation of rifampicin in Mycobacterium tuberculosis. *Access Microbiol.* **1** (2019).

767 62. L. J. V. Piddock, K. J. Williams, V. Ricci, Accumulation of rifampicin by Mycobacterium
768 aurum, Mycobacterium smegmatis and Mycobacterium tuberculosis. *J. Antimicrob.*
769 *Chemother.* **45**, 159–165 (2000).

770 63. Y. Bhusal, C. M. Shiohira, N. Yamane, Determination of in vitro synergy when three
771 antimicrobial agents are combined against Mycobacterium tuberculosis. *Int. J.*
772 *Antimicrob. Agents* **26**, 292–297 (2005).

773 64. M. S. Pavelka, W. R. Jacobs, Biosynthesis of diaminopimelate, the precursor of lysine
774 and a component of peptidoglycan, is an essential function of Mycobacterium
775 smegmatis. *J. Bacteriol.* **178**, 6496–6507 (1996).

776 65. J. Lee, T. Repasy, K. Papavinasasundaram, C. Sassetti, H. Kornfeld, Mycobacterium
777 tuberculosis Induces an Atypical Cell Death Mode to Escape from Infected
778 Macrophages. *PLOS ONE* **6**, e18367 (2011).

779 66. T. Metsalu, J. Vilo, ClustVis: a web tool for visualizing clustering of multivariate data
780 using Principal Component Analysis and heatmap. *Nucleic Acids Res.* **43**, W566–W570
781 (2015).

782 67. V. Matyash, G. Liebisch, T. V. Kurzchalia, A. Shevchenko, D. Schwudke, Lipid extraction
783 by methyl-tert-butyl ether for high-throughput lipidomics. *J. Lipid Res.* **49**, 1137–1146
784 (2008).

785

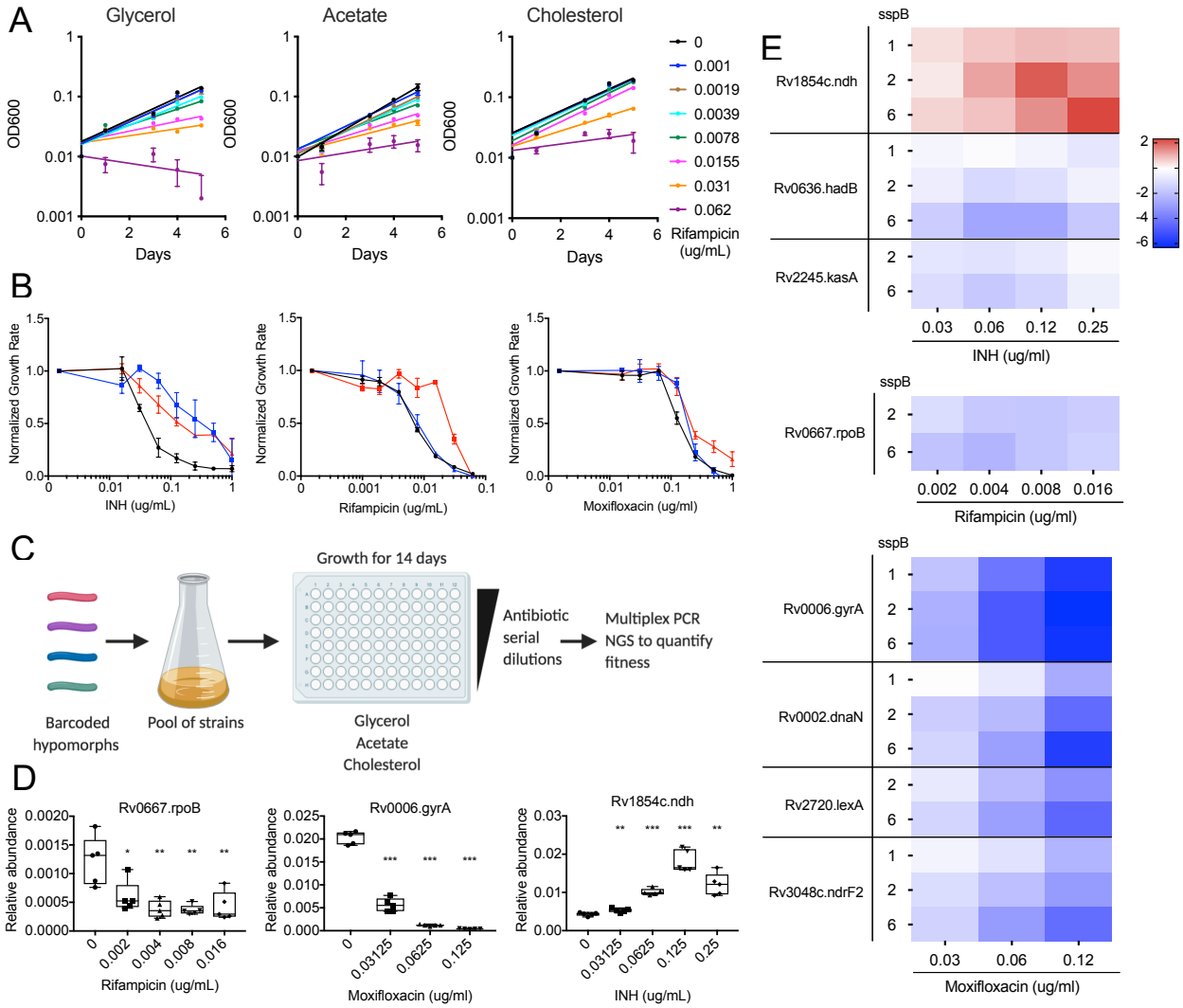

Figure 1. Genetic strategy to define essential bacterial functions that alter drug efficacy *in vitro*. (A) Growth of H37Rv in minimal media with glycerol, acetate and cholesterol as the sole carbon source and increasing concentrations of RIF. Results shown as mean from 3 biological replicates with standard deviations. **(B)** Normalized growth inhibition of WT *Mtb* across increasing concentrations of INH, RIF and MOX in minimal media with glycerol (black), acetate (blue) and cholesterol (red) as sole carbon sources. Results shown as means from 3 biological replicates with standard deviations. **(C)** Barcoded hypomorph mutants were pooled and grown in 96-well plates containing

795 minimal media with glycerol, acetate or cholesterol as the sole carbon source for 14
796 days. Antibiotics were added to individual wells as well as untreated controls.
797 Chromosomal barcodes were PCR amplified and pooled for Illumina Next Generation
798 Sequencing (NGS). Barcodes were analyzed to quantify changes in fitness of individual
799 strains from different conditions. **(D)** Boxplot representing changes in relative
800 abundances of *rpoB***,** *gyrA* and *ndh* mutants grown in glycerol during RIF, MOX and INH
801 treatment respectively. The highest drug concentration tested for RIF, MOX and INH
802 represent the concentration at which most of the strains in the library were inhibited.
803 Data represents 5 biological replicates. Significance was calculated using unpaired t-
804 test and compared to untreated conditions, *$p<0.05$, **$p<0.01$, ***$p<0.001$. **(E)** Heat map
805 representing changes in fitness of individual mutants, shown as Log2 fold change,
806 during INH, RIF and MOX treatment in glycerol growth conditions. Mutants were chosen
807 from previous association with respective antibiotic. sspB numbers denote *sspB*
808 expression level of mutant. Results shown as means from 5 biological replicates.
809
810

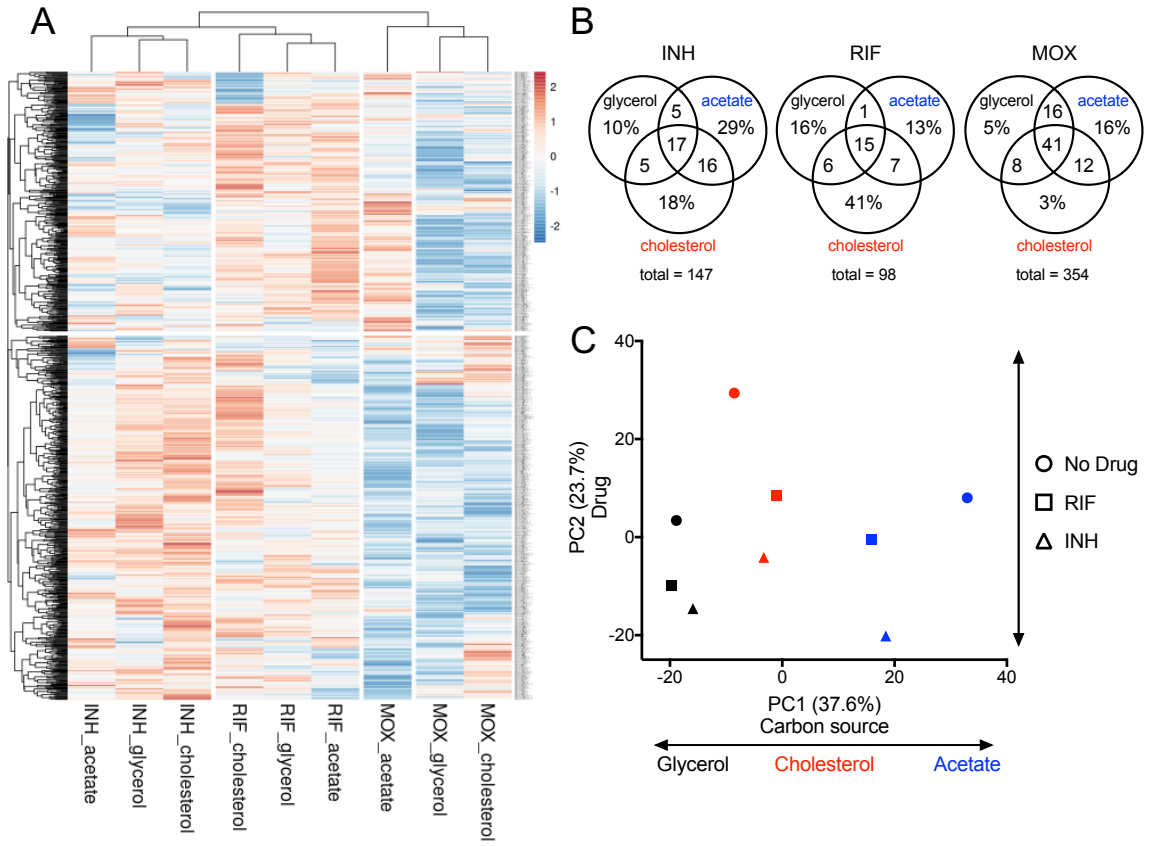

Figure 2. Carbon sources mediate antibiotic-genetic interactions of essential bacterial functions. (A) Heat map of hypomorph mutants shown as Log2 fold change of 0.65X GR_{50} of INH, RIF and MOX against untreated controls. Results shown as means from 5 biological replicates. Each antibiotic (INH, RIF and MOX) in single carbon source (glycerol, acetate and cholesterol) conditions were compared using hierarchical clustering methods. **(B)** Venn diagrams showing the total number of genes with log2FC > -1 and $p<0.05$ at 0.65X GR_{50} of INH, RIF and MOX, and the % of genes associated with specific conditions. (**C)** Relative abundance datasets of the hypomorph libraries from glycerol (black), acetate (blue) and cholesterol (red) growth conditions with 0.65X GR_{50} INH (triangle) and RIF (square) treatment as well as untreated controls (circle)

822 were examined using principal component analysis. Units shown on axes are arbitrary

823 values in principal component space.

824

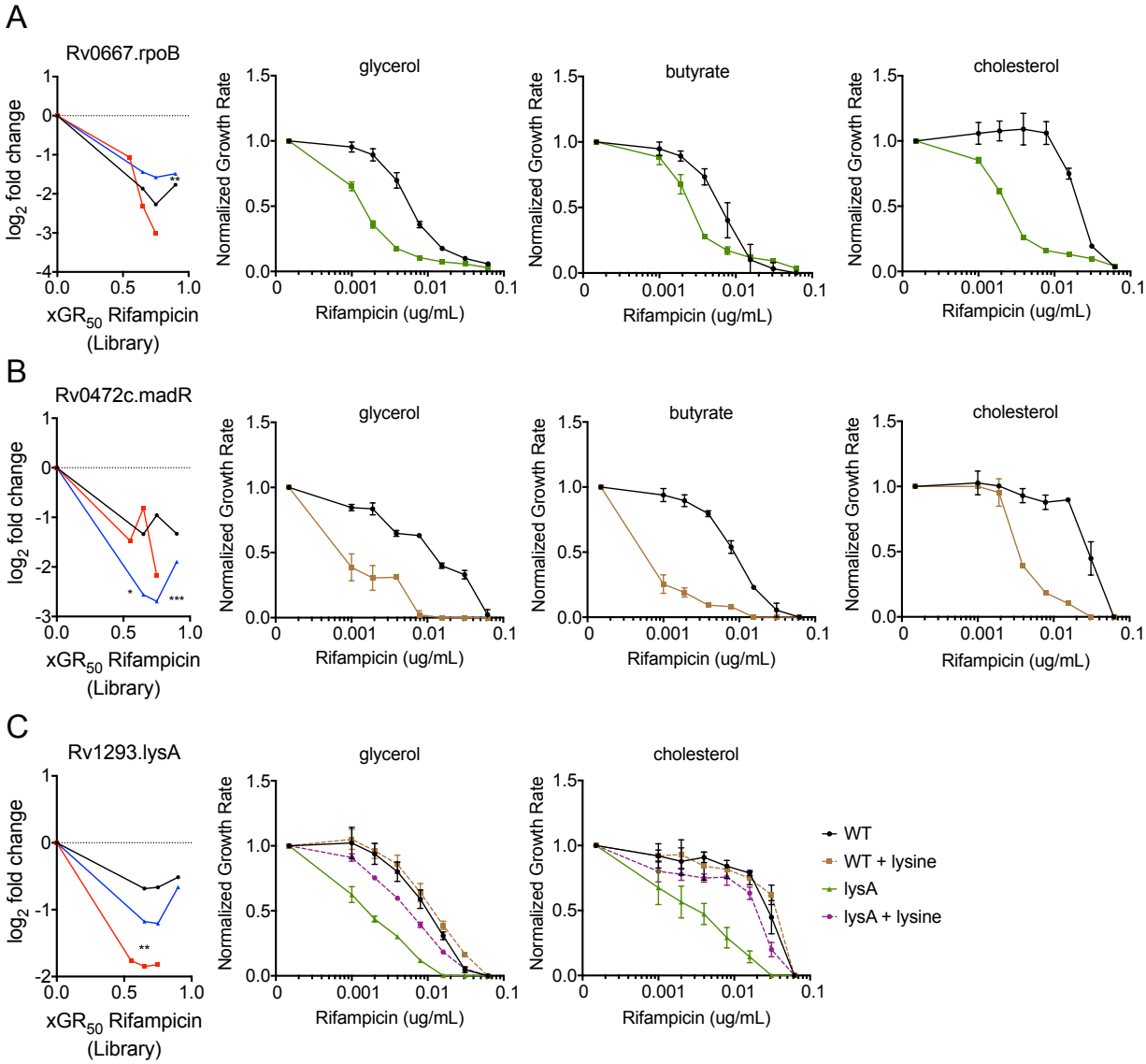

825

826 **Figure 3. Condition-independent chemical-genetic interactions can be reproduced**
827 **with individual mutants. (A)** RpoB depletion shows decreased fitness compared to the
828 library over increasing concentrations of RIF for glycerol (black), acetate (blue) and
829 cholesterol (red). Normalized growth inhibition assay shows *rpoB* hypomorph mutant
830 (green) has decreased RIF MIC compared to WT (black) across multiple carbon
831 conditions. **(B)** MadR depletion shows decreased fitness compared to the library over
832 increasing concentrations of rifampicin for glycerol (black), acetate (blue) and

833 cholesterol (red). Normalized growth inhibition assay shows *madR* hypomorph mutant
834 (brown) has decreased RIF MIC compared to WT (black) across multiple carbon
835 conditions. **(C)** LysA depletion shows decreased fitness compared to the library over
836 increasing concentrations of rifampicin for glycerol (black), acetate (blue) and
837 cholesterol (red). Normalized growth inhibition assay shows *lysA* hypomorph mutant
838 (green) has decreased RIF MIC compared to WT (black), which can be reversed by
839 3mM lysine supplementation (purple). Library results are shown as means from 5
840 biological replicates, and significance was calculated using unpaired t-test with
841 Benjamini-Hochberg multiple testing correction, *q<0.05, **q<0.01, ***q<0.001.
842 Normalized growth inhibition results are shown as means from 3 biological replicates
843 with standard deviations.
844
845

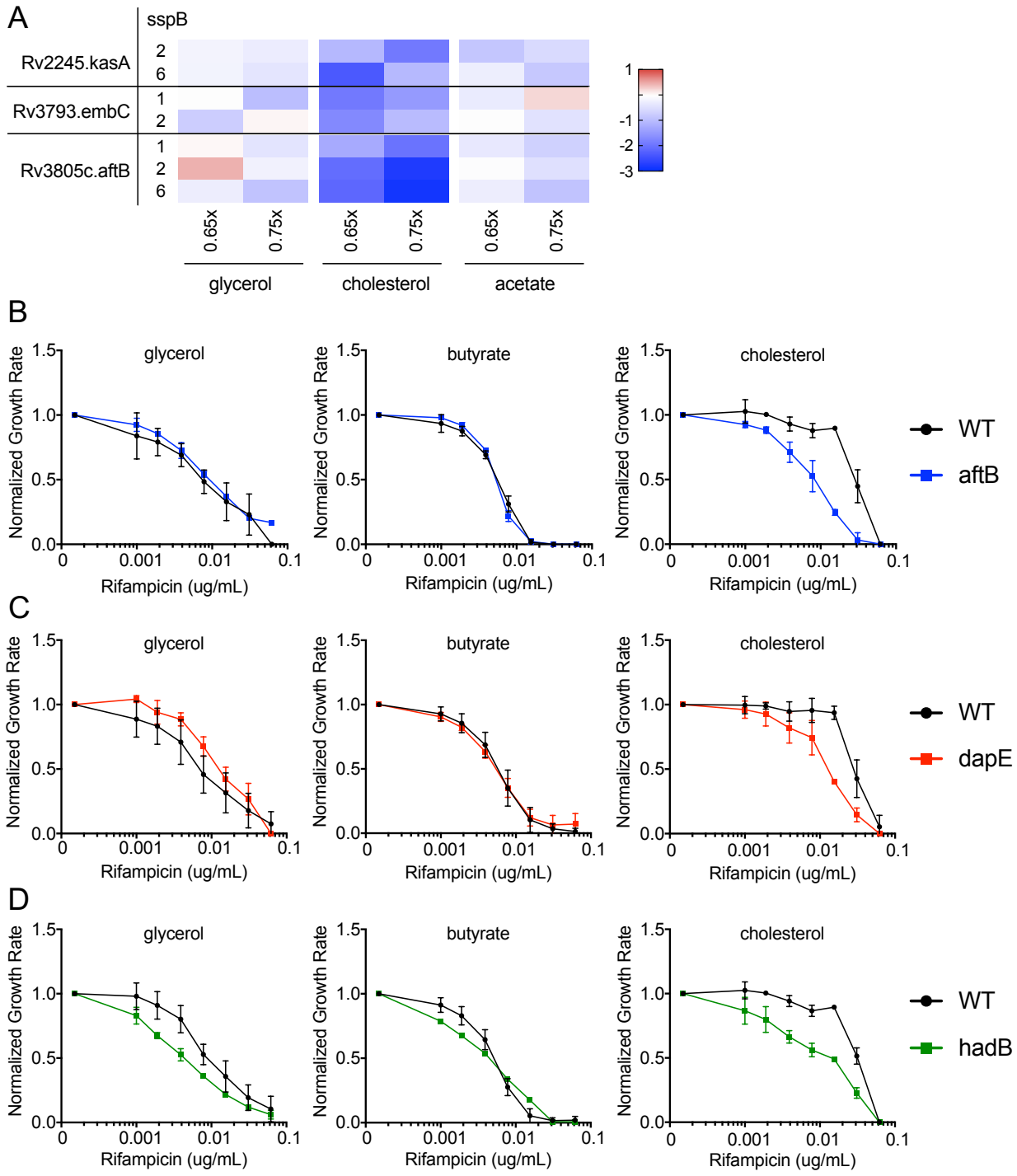

846

847 **Figure 4. Cell-wall biosynthesis hypomorph mutants show altered RIF efficacy**

848 **during cholesterol growth conditions. (A)** Heat map showing hypomorph mutants of

849 select mycobacterial cell-wall biosynthesis genes and pathways with significant changes

850 in fitness during cholesterol growth, shown as Log2 fold change at 0.65X and 0.75X
851 GR_{50} of RIF against untreated controls. Results shown as means from 5 biological
852 replicates. Classification of mutants was done using Mycobrowser. **(B-D)** Normalized
853 growth inhibition of WT and select mutants across increasing concentrations of RIF in
854 minimal media with sole carbon sources. Depletion of AftB (blue), DapE (red) and HadB
855 (green) show decreased RIF MIC compared to WT (black) only during cholesterol
856 growth conditions. Results shown as means from 3 biological replicates with standard
857 deviations.
858
859

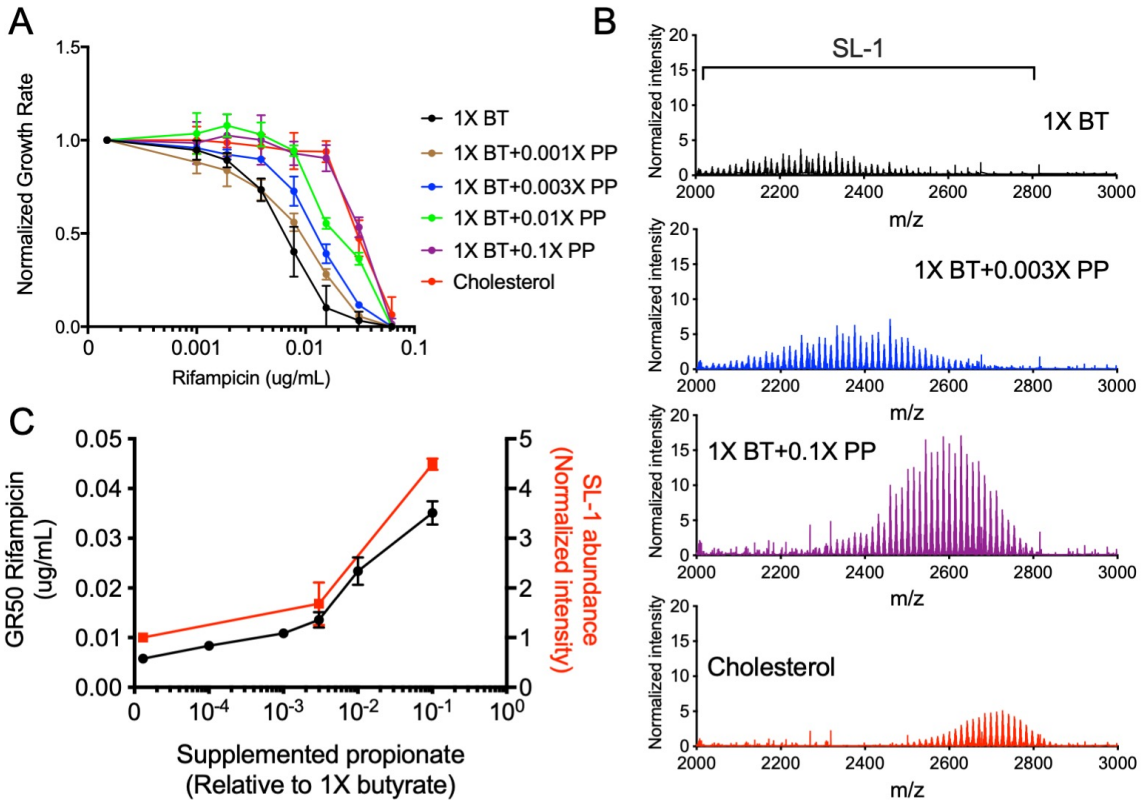

Figure 5. Propionate and cholesterol catabolism decreases RIF efficacy in correlation with increased branched chain lipid length and abundance. (A) Normalized growth inhibition of WT across increasing concentrations of RIF in minimal media with 1X butyrate (BT) and corresponding propionate (PP) supplementations as well as cholesterol. Results shown as means from 3 biological replicates with standard deviations. **(B)** Mass spectra of total lipid extract from WT grown in minimal media with 1X butyrate (BT) and corresponding propionate (PP) supplementations as well as cholesterol. MS spectra intensities were normalized using GM2 ganglioside internal standard and cell density. Results shown as representative from 2 independent experiments. Mass range characteristic of sulfolipid-1 is shown. **(C)** Plotted GR_{50} values (black) and relative sulfolipid abundances (red) across increasing propionate levels. Relative sulfolipid abundances were determined by the combined normalized mass

spectra intensities from *m/z* 2000-2800 for each growth condition. Results shown as means with standard deviations.

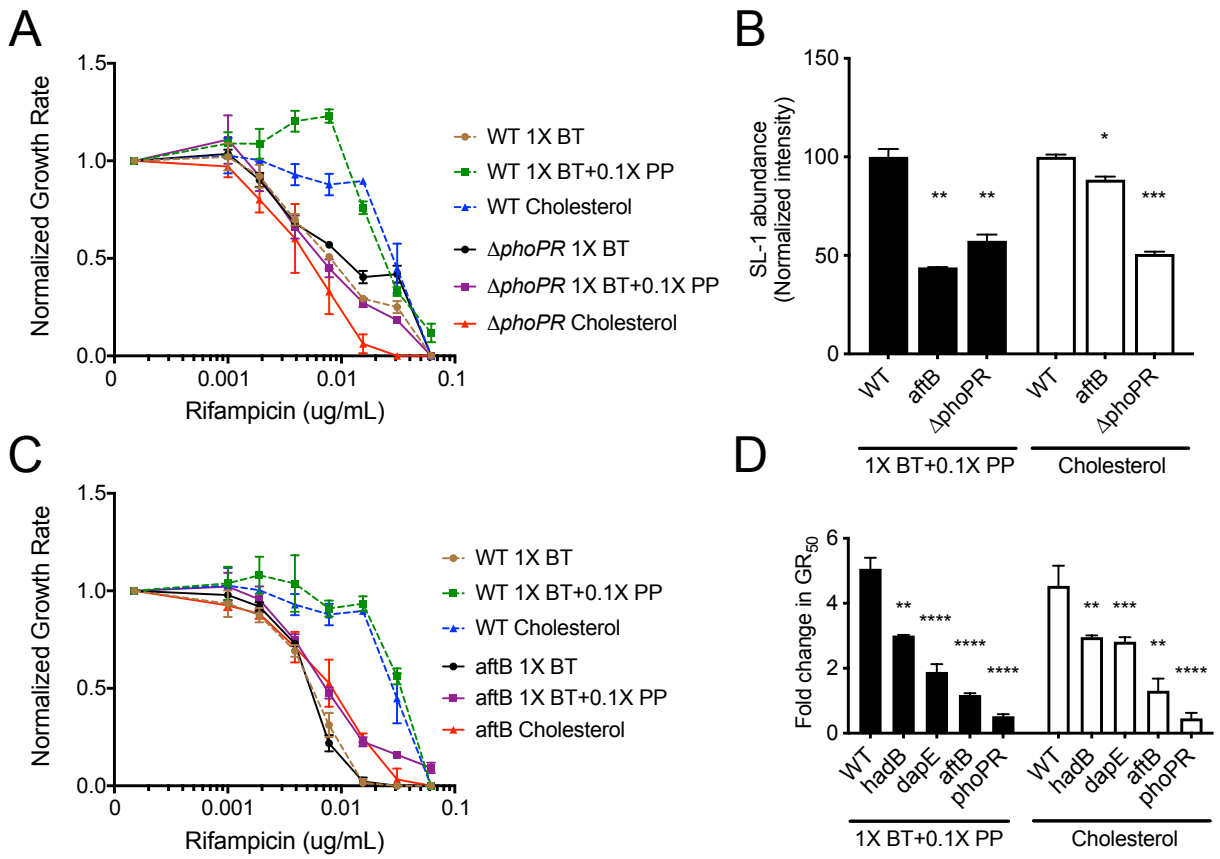

Figure 6. Disruption of the cell envelope reverses propionate and cholesterol catabolism dependent decrease in RIF efficacy. (A) Normalized growth inhibition of Δ*phoPR* mutant across increasing concentrations of RIF in minimal media compared to WT. Results shown as means from 3 biological replicates. **(B)** Relative sulfolipid abundances of WT, *aftB* mutant and Δ*phoPR* mutant grown in minimal media with 1X butyrate and 0.1X propionate (1X BT+0.1X PP), and cholesterol. Relative sulfolipid abundances were determined by the combined normalized mass spectra intensities from *m/z* 2000-2800 for each growth condition. MS spectra intensities were normalized using GM2 ganglioside internal standard and cell density. Results shown as means with standard deviations from 2 independent experiments. Significance was calculated using unpaired t-test, *p<0.05, **p<0.01. **(C)** Normalized growth inhibition of *aftB* mutant

890 across increasing concentrations of RIF in minimal media compared to WT. Results

891 shown as means from 3 biological replicates. **(D)** Calculated fold change in GR_{50} values

892 of 1X butyrate and 0.1X propionate (1X BT+0.1X PP) and cholesterol conditions against

893 1X butyrate alone for WT and mutant strains. Significance was calculated using

894 unpaired t-test, ***p*<0.01, ****p*<0.001, *****p*<0.0001.

895

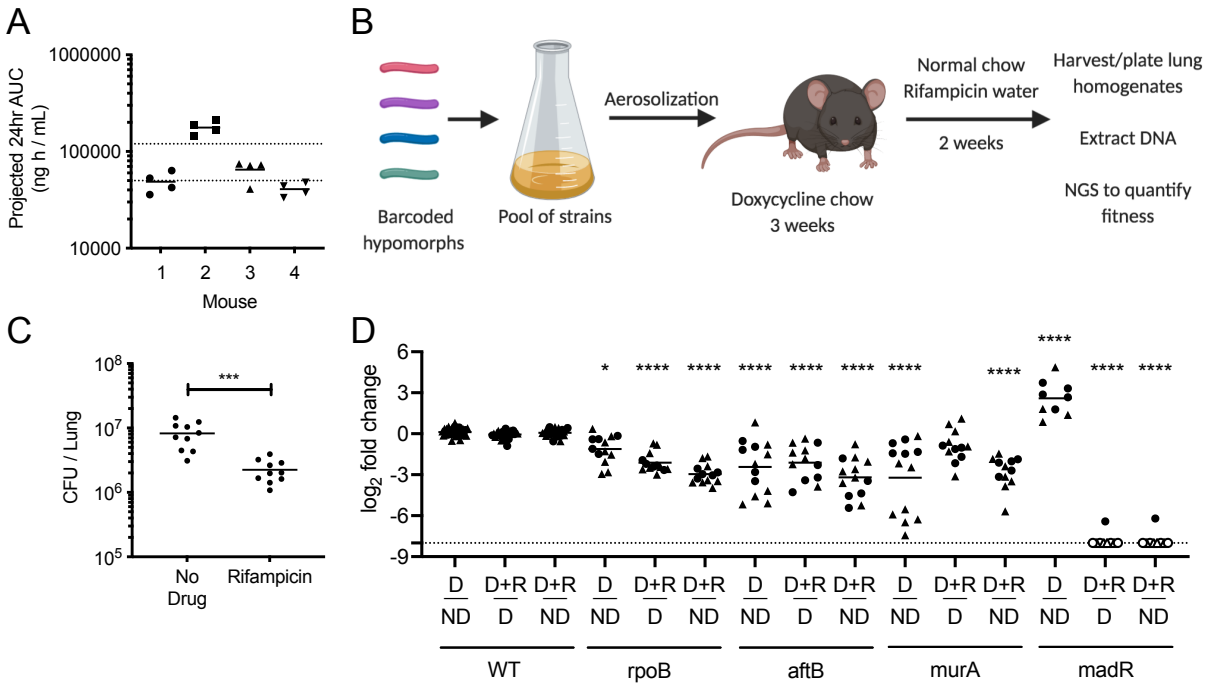

Figure 7. Essential bacterial functions that alter drug efficacy *in vivo*. (A) RIF plasma concentrations were measured in mice over 12-hour period 24 hours post RIF administration (0.1g/L). Results shown as Area Under the Concentration (AUC) time profile. Dotted lines indicate RIF plasma range observed during clinical TB therapy (58). **(B)** C57BL/6J mice were infected through the aerosol route with a pooled culture of individual hypomorph mutants and barcoded WT strains. Mice were fed doxycycline chow starting 3 days before infection to 3 weeks post infection. Mice were subsequently switched to normal chow and water with or without RIF (0.1g/L) for 2 additional weeks. Lungs were harvested, homogenized and plated for *Mtb* outgrowth. Upon DNA extraction of grown colonies, chromosomal barcodes were PCR amplified and pooled for Illumina Next Generation Sequencing (NGS). Barcode abundances of individual mutants were normalized to WT strains and analyzed to quantify changes in fitness during RIF treatment. **(C)** RIF treated mice show significant decrease in *Mtb* CFU in

910 lungs compared to untreated controls. Each dot represents a single mouse. Significance
911 was calculated using unpaired t-test, ***p<0.001. **(D)** Change in fitness of individual
912 mutants were determined by comparing normalized counts from non-depleted (ND),
913 depleted (D) as well as depleted and RIF treated (D+R) conditions. Depletion of RpoB,
914 AftB and MurA display significant decrease in fitness, shown as Log2 fold change,
915 compared to non-depleted controls. Depletion of RpoB, AftB and MadR show significant
916 decrease in fitness during RIF treatment compared to depleted but untreated controls.
917 Results shown as two independent experiments (circle, triangle) with each dot
918 representing a single mouse. Empty dot indicates that the relative abundance was
919 below the limit of detection (Dotted line). Significance was calculated using Sidak's
920 multiple comparison test, *p<0.05, ****p<0.0001.
921